Atomic hydrogen interactions with gas-phase coronene cations hydrogenation versus fragmentation

Rapacioli, Mathias; Cazaux, Stéphanie; Foley, Nolan; Simon, Aude; Hoekstra, Ronnie; Schlathölter, Thomas

DOI
10.1039/c8cp03024c

Publication date
2018

Document Version
Final published version

Published in
Physical Chemistry Chemical Physics

Volume 20 | Number 35 | 21 September 2018 | Pages 22397–23154

PCCP

Physical Chemistry Chemical Physics

rsc.li/pccp

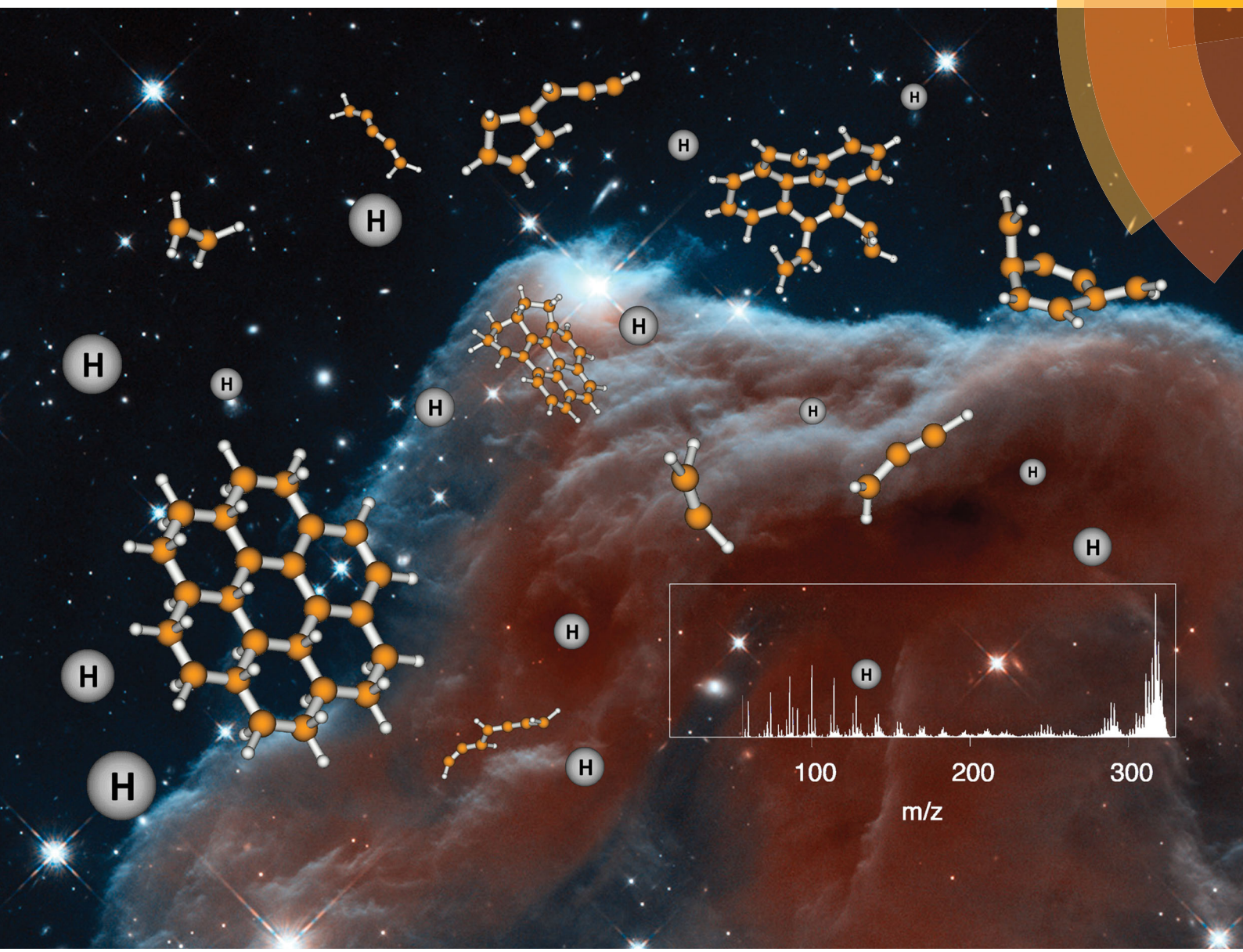

ISSN 1463-9076

ROYAL SOCIETY OF CHEMISTRY

PAPER

Mathias Rapacioli *et al.*

Atomic hydrogen interactions with gas-phase coronene cations: hydrogenation *versus* fragmentation

PCCP

PAPER

View Article Online
View Journal | View Issue

Cite this: *Phys. Chem. Chem. Phys.*, 2018, **20**, 22427

Atomic hydrogen interactions with gas-phase coronene cations: hydrogenation *versus* fragmentation

Mathias Rapacioli, †*[a] Stéphanie Cazaux,†[bc] Nolan Foley,[d] Aude Simon,[a] Ronnie Hoekstra[d] and Thomas Schlathölter[d]

Received 11th May 2018,
Accepted 19th June 2018

DOI: 10.1039/c8cp03024c

rsc.li/pccp

Sequential hydrogenation of polycyclic aromatic hydrocarbon (PAH) cations drives a gradual transition from a planar to a puckered geometry and from an aromatic to an aliphatic electronic structure. The resulting H-induced weakening of the molecular structure together with the exothermic nature of the consecutive H-attachment processes can lead to substantial molecular fragmentation. We have studied H attachment to gas-phase coronene cations in a radiofrequency ion trap using tandem mass spectrometry. With increasing hydrogenation, C_2H_i loss and multifragmentation are identified as main de-excitation channels. To understand the dependence of both channels on H-exposure time, we have simulated the molecular stability and fragmentation channels of hydrogenated PAHs using a molecular dynamics approach employing potential energies determined by a density functional based tight binding method. As the coronene fragmentation patterns depend on the balance between energy deposition by H-attachment and the extent of cooling in between subsequent attachment processes, we investigate several scenarios for the energy distribution of hydrogenated PAHs. Good agreement between experiment and simulation is reached, when realistic energy distributions are considered.

1 Introduction

The understanding of hydrogen attachment to carbon surfaces and, as a nanoscale representative, to polycyclic aromatic hydrocarbons (PAHs) is essential to a wide variety of research fields and technologies such as hydrogen storage for transportation, electronic devices and the formation of H_2 in space. One of the fascinating properties of PAHs is their ability to accommodate atomic hydrogen. In principle, every C atom in a PAH can be hydrogenated but attachment barriers and binding energies are strongly site dependent[11] and change as the molecule gradually transits from a fully aromatic electronic structure, to an aliphatic one. During this transition, the planar geometry of a pristine PAH is modified towards the puckered geometry of the fully hydrogenated system and the molecule is structurally weakened.

In the condensed phase, H attachment to PAHs is interesting as a model system for hydrogen interactions with graphene. In graphene, hydrogenation of a C atom changes its hybridization from sp^2 to sp^3. As a result a bandgap is opened,[1] which is required for the use of graphene as a semiconductor. H interactions with graphene are also fundamental for graphene based hydrogen storage.

From an astrochemical perspective, hydrogenation of neutral PAHs and their ions in the gas phase is a key reaction to be investigated. The Aromatic Infrared Bands (AIBs), which are a common feature of a multitude of astrophysical objects within our galaxy and beyond are commonly associated to PAHs.[2,3] An unambiguous identification of specific PAH-based systems from the AIBs remains difficult. However, entire families of astronomical PAHs have already been identified,[4,5] both as neutrals or as positive ions.[8] These PAHs are often thought to be hydrogenated and considered as catalysts for H_2-formation.[6] The presence of pre-adsorbed H atoms on PAHs increases the yield of H_2 formation by many orders of magnitude,[7] rendering this process an important route towards molecular hydrogen formation in the interstellar medium (ISM).[8]

Pioneering laboratory studies have focused on the hydrogenation of graphite and graphene surfaces and on PAH thin films,[9] for which PAH superhydrogenation was experimentally observed for the first time. More recently, hydrogenation of

[a] *Laboratoire de Chimie et Physique Quantiques LCPQ/IRSAMC, UMR5626, Université de Toulouse (UPS) and CNRS, 118 Route de Narbonne, F-31062 Toulouse, France*
[b] *Faculty of Aerospace Engineering, Delft University of Technology, Kluyverweg 1, 2629 HS, Delft, The Netherlands*
[c] *University of Leiden, P.O. Box 9513, NL, 2300 RA, Leiden, The Netherlands*
[d] *Zernike Institute for Advanced Materials, University of Groningen, Nijenborgh 4, 9747AG Groningen, The Netherlands*
† These authors contributed equally to this work.

coronene cations in the gas-phase was observed using radio-frequency ion traps.[10] A subsequent study revealed that H attachment follows a site-selective sequence *via* "magic" hydrogenation states of particular stability.[11]

The Stockholm group and the Groningen group have debated whether additional hydrogen atoms stabilize or destabilize PAH integrity upon interaction with photons or in collisions. For moderate hydrogenation, Reitsma *et al.* found an increase in stability of coronene cations upon soft X-ray photoabsorption.[12] On the other hand, for laser induced dissociation of the smaller PAH cation pyrene, already the addition of 6 H atoms decreases stability towards C-backbone fragmentation.[13] Gatchell *et al.* found a similar structural weakening of pyrene cations in collisions with 300 eV He atoms.[14]

As hydrogen attachment to PAH cations is an exothermic process, it is also possible that sequential hydrogenation itself can induce fragmentation. This is not a relevant process for hydrogenation in astrophysical environments, where subsequent H attachment events to the same PAH molecule will typically be separated by astronomical timescales that leave sufficient time for de-excitation. In the laboratory, however, partial H pressures are such that multiple hydrogenation is usually accomplished within a few seconds, *i.e.* the increase of internal energy due to H attachment competes with energy loss due to different cooling processes.

In the following we investigate this interplay in a combined experimental and theoretical study.

2 Experiments

2.1 Experimental setup

The experiments have been performed using a versatile tandem-mass spectrometer that we have developed for the investigation of dynamics in complex molecular ions.[10,15] The setup is shown schematically in Fig. 1. We used electrospray ionization to transfer ions from a solution into the gas phase. Based on the method of Maziarz *et al.*,[16] 600 μL of a saturated solution of coronene in methanol was diluted with 350 μL HPLC-grade methanol. 50 μL of a 10 mM $AgNO_3$ solution in methanol was added to facilitate electron transfer from coronene molecules to silver ions, leading to formation of the coronene radical cations ($[C_{24}H_{12}]^+$, m/z = 300) in solution. A beam of these ions was extracted from an electrospray ion source at atmospheric pressure. The ions were phase-space compressed in a radio-frequency (RF) ion funnel and transported by an RF 8-pole ion guide. The mass selection has been performed by using an RF quadrupole mass filter. Accumulation of the ions took place in a three-dimensional RF ion trap (Paul trap), assisted by a pulse of He buffer gas (at 300 K), facilitating trapping by collisional cooling.

The thermal beam of atomic hydrogen was produced from H_2 using a Slevin-type RF-discharge source[17] which has been previously used in crossed beam experiments.[18,19] The atomic H source was interfaced with the 3D RF trap vacuum chamber, to be able to follow the hydrogenation as a function of H exposure time τ_{exp}. Typical dissociation fractions in the trap center were around 0.3 and the thermal energy of the produced H beam was around 25 meV.

The m/z distribution of the trapped ions was determined by pulsed extraction into a time-of-flight (TOF) mass spectrometer with a resolution $M/\Delta M \sim 300$. We typically accumulated a few hundred TOF traces to reach sufficient statistics. (Multiple) H attachment manifests in the mass spectrum as peaks with $m/z > 300$ whereas fragmentation due to H interactions leads to peaks with $m/z < 300$. We operated the RF trap at a low mass cutoff of about 60 Da.

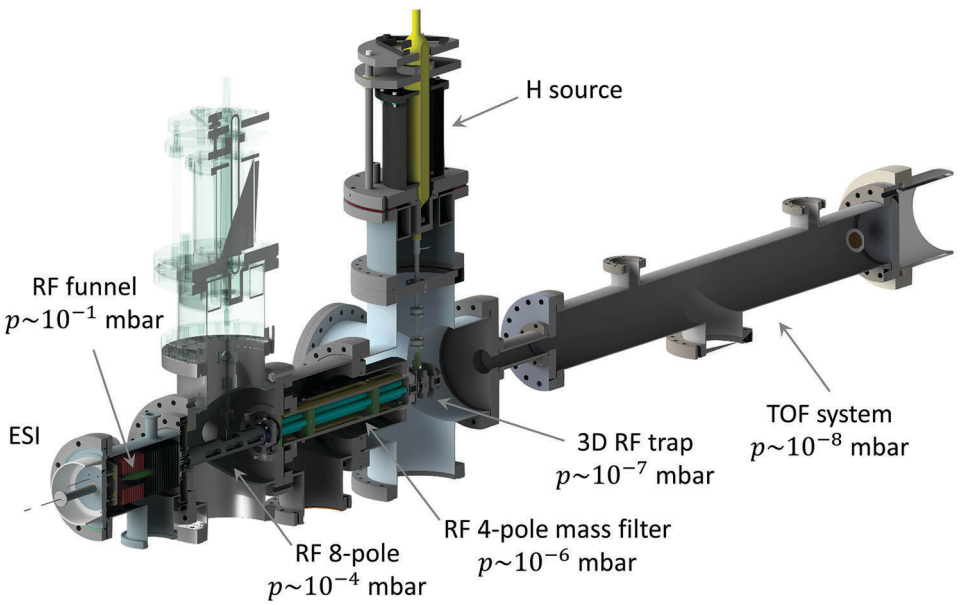

Fig. 1 Experimental setup for the controlled hydrogenation of PAH ions. The atomic H source can either be attached to the RF 8-pole chamber (semi-transparent) or to the 3D RF trap chamber.

2.2 Experimental results

We have already discussed the general characteristics of the evolution of coronene hydrogenation with H-exposure time τ_{exp} in a previous publication.[11] Gas phase coronene cations exposed to a constant flux of H atoms can be hydrogenated up to the fully hydrogenated state where 24 H atoms are attached (corresponding to a peak at 324 Da in the mass spectra). The degree of hydrogenation increased monotonically with H-exposure time. This is shown in Fig. 2 that displays the evolution of the mass spectra for exposure times from 0 to 59 s. Upon H exposure, the m/z distribution above 300 Da exhibits a shift to higher masses, accompanied by a broadening of the distribution. This can be clearly seen in Fig. 3 (right panels). Also, it should be noted that odd m/z values dominate the spectrum. As mentioned in our previous work, the hydrogenation of coronene cations shows the predominance of cations with either 5, 11 or 17 extra hydrogen atoms, which we refer to as magic numbers (shown as m/z = 305, 311 and 317 in Fig. 3). These particular hydrogenation states are very prominent in the different mass spectra, especially for the highest exposure times. By static DFT calculations it was shown that the magic-number systems exhibit particularly high binding energies.[11]

In the present study we focus on the interplay between hydrogenation of coronene cations and their fragmentation, the latter resulting in systems with masses lower than the coronene precursor at m/z = 300 (see Fig. 2). Early vacuum ultraviolet (VUV) photofragmentation studies on PAH cations[20] have already shown that the fragmentation channels with lowest activation energies are typically H-loss, H_2-loss and C_2H_2-loss with lowest activation energies typically found for H-loss and highest activation energies for C_2H_2-loss. In collision experiments with keV ions, substantially higher PAH internal energies can be reached and besides the previously observed channels, multifragmentation into a variety of small hydrocarbon molecules is observed.[21,22] Low energy atomic collisions enable non-statistical C-knockout processes[23] and even statistical CH_m-loss.

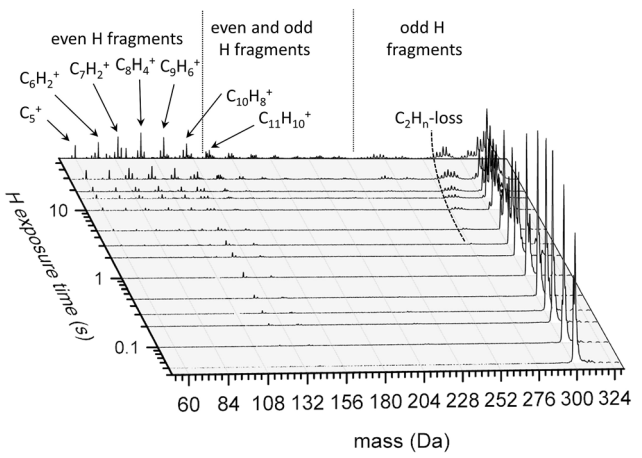

Fig. 2 Mass spectra for hydrogenation of $[C_{24}H_{12}]^+$ cations as a function of H exposure time. Contamination peaks at 106.9 and 108.9 ($^{107}Ag^+$ and $^{109}Ag^+$ from the ESI source) have been removed.

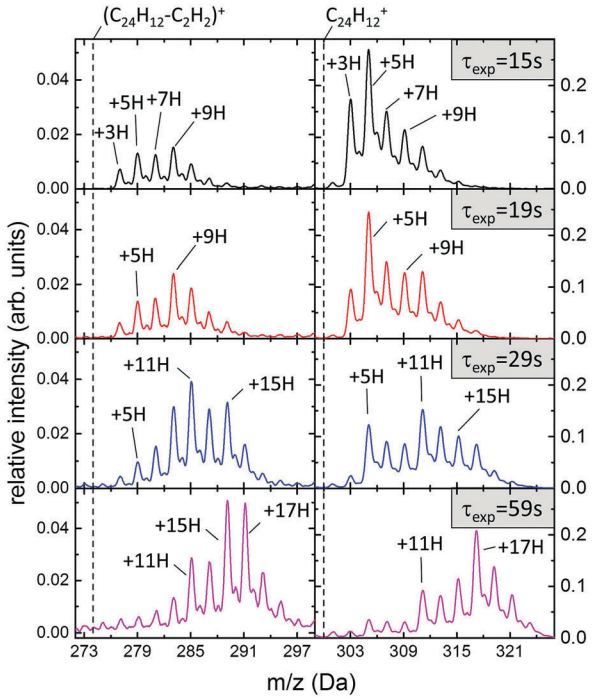

Fig. 3 Co-evolution of the $[C_{24}H_{12} + nH]^+$ distribution (right panel, m/z = 300–324) and of the $[C_{24}H_{12} + nH - C_2H_i]^+$ distribution as a function of H-exposure time (τ_{exp} = 15–59 s). The dashed lines indicate m/z = 300 (right, $C_{24}H_{12}^+$) and m/z = 274 (left, $[C_{24}H_{12}-C_2H_2]^+$).

From Fig. 2 it is obvious that sequential H attachment can lead to multifragmentation and to C_2H_i loss. Loss of H and H_2 cannot be clearly identified, as it interferes with H attachment and no evidence for CH_2 loss is observed.

2.3 C_2H_2-loss

For VUV photoionization of neutral PAHs, C_2H_2 loss is a well defined dissociation channel.[20] Sequential hydrogenation of coronene cations, however, leads to a different scenario. Hydrogen attachment is an exothermic process that increases the internal energy of the resulting molecular ion. As discussed later in this article, the balance between internal energy increase due to hydrogen attachment and radiative cooling is a statistical quantity that depends on the atomic H flux. Accordingly, loss will typically originate from a multiply hydrogenated system $[C_{24}H_{12} + nH]^+$ with nH broadly distributed. Furthermore, fragment ions are generally exposed to H atoms for the remaining trapping time, and can be hydrogenated as well. Consequently, the loss channel is less well defined and will be referred to as C_2H_i-loss, as the precursor n is never well defined. Experimental results are shown in Fig. 3 for H-exposure times τ_{exp} = 15–59 s, where fragmentation is a very relevant channel. The right panel shows the m/z = 299–326 Da range of the hydrogenated precursor. The $[C_{24}H_{12} + nH]^+$ distribution peaks at n = 5 (τ_{exp} = 19 s), n = 11 (τ_{exp} = 29 s) and n = 17 (τ_{exp} = 59 s). The mass spectra are all dominated by odd values of n, reflecting the small or non-existing barriers for H attachment found for even n species (radical-radical reaction).[11] The left panel of Fig. 3

shows the m/z = 272–299 amu range with the respective C_2H_i loss peaks. As for their hydrogenated precursors, odd m/z values dominate. The ratio between loss peaks and precursor peaks increases with τ_{exp}, reflecting the increase in internal energy. Most importantly, the C_2H_i distribution exhibits a very similar trend as observed for the precursor: with increasing τ_{exp}, successive H attachment shifts the distribution to higher m/z. For τ_{exp} = 59 s, the $[C_{24}H_{12} + nH–C_2H_i]^+$ distribution is qualitatively very similar to the $[C_{24}H_{12} + nH]^+$ distribution, with the exception of a relatively strong nH = 15 peak. For lower exposure times the agreement is less good and in general, the $[C_{24}H_{12} + nH–C_2H_2]^+$ distribution is shifted to higher n than the precursor distribution. This finding could be due to lowering of H-attachment barriers upon C_2H_i loss. As might be expected, the coronene magic numbers do not seem to be conserved upon C_2H_i loss.

2.4 Multifragmentation

Fig. 4 displays the m/z = 60–180 Da mass range for H-exposure times τ_{exp} = 1–59 s. Note that smaller m/z values are not detected in our experiment, as the RF trap has its low m/z cutoff just below this range. The first clearly distinguishable fragments at m/z = 124 Da and at m/z = 141 Da are visible already after 1 s (albeit of very low relative intensity). No evidence for doubly charged ions is observed. It is generally difficult to assign molecular structures to multifragmentation peaks. Possibly, both peaks are due to double ring structures such as the tetradehydronaphthalene cation (m/z = 124) and naphthalenemethylium (m/z = 141). For τ_{exp} = 3 s, peaks at smaller m/z values start to appear. For each number of C atoms, a particular H number is dominating and the strongest peaks are $C_6H_2^+$, $C_7H_2^+$, $C_8H_4^+$ and $C_9H_6^+$. $C_6H_2^+$ and $C_7H_2^+$ both contain only 2 H atoms, which hints at a linear geometry. $C_8H_4^+$ as well as $C_9H_6^+$ are more hydrogenated and their geometry is probably based on a single 6 membered C ring.

A less obvious feature of the spectra in Fig. 4 is a subtle shift of fragment masses to lower m/z with increasing exposure time τ_{exp}. The strongest peak at τ_{exp} = 1 s is found at m/z = 124 Da whereas at τ_{exp} = 59 s, the strongest peak is at m/z = 100 Da.

Fig. 5 shows a zoom into the $C_lH_m^+$ groups of peaks for l = 5–11 for τ_{exp} = 15–59 s. Besides the dominating peaks that were discussed in the last paragraph, a remarkable finding is the dominance of even m fragments over the entire mass range. The sole exception is the $C_{11}H_9^+$ peak at m/z = 141. On the other hand, a predominance of odd m/z species is found for $m/z \geq 139$, as already discussed for $[C_{24}H_{12} + nH]^+$ and $[C_{24}H_{12} + nH–C_2H_2]^+$. Between the low and even m/z range and the high and odd m/z range, a broad distribution of peaks is found where even and odd m/z values co-exist.

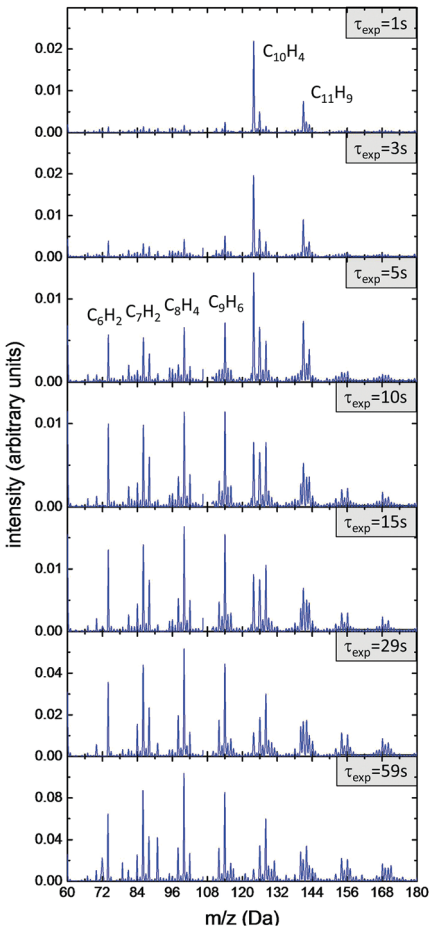

Fig. 4 Multifragmentation pattern as a function of H-exposure time (experimental data). The Y-axis range increases with exposure time τ.

2.5 H flux

As the experiments are conducted at high vacuum pressures, the atomic H can be approximated as an ideal gas. The H impact rate on the surface of a coronene cation should then be well described by the collision flux Z determined using kinetic theory which scales linearly with pressure p. Experimentally, Z can then be kept constant by keeping $p \times \tau_{exp}$ constant and the effect of the flux can be investigated by variation of p and τ_{exp}. The parameters for the data presented in Fig. 6 were chosen such that very similar coronene hydrogenation patterns are reached at 3 different H pressures. It is obvious, that for these circumstances, the product of p and τ_{exp} is not the same. Furthermore, relative yields for C_2H_i loss decreases with decreasing pressure whereas multifragmentation increases. This highlights how the variation of the time between two H additions influences the fragmentation. Increasing this time allows the system to cool in between consecutive H addition and less fragmentation occurs.

To precisely quantify fragmentation and C_2H_i loss as a function of mean degree of coronene hydrogenation, we have first determined the mean hydrogenation $\bar{n}$ from the data displayed in Fig. 2 by integration of the respective hydrogenation peaks. The peak areas are used to calculate $\bar{n}$. The results are displayed in Fig. 7a. Hydrogenation increases approximately with the square root of the exposure time $\tau^{1/2}$. Fig. 7b then gives the survival yield as a function of mean hydrogenation, as defined by

$$Y_{survival} = \frac{Y_{cor+nH}}{Y_{cor+nH} + Y_{cor-C_2H_i} + Y_{fragments}} \quad (1)$$

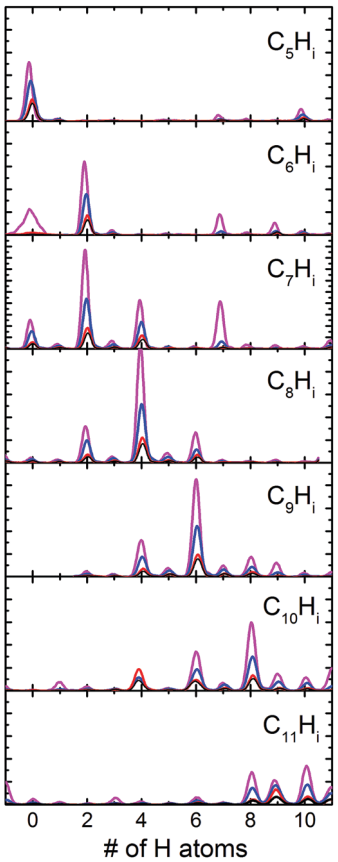

Fig. 5 $C_mH_i^+$ distribution for m = 5 (top) to m = 11 (bottom). The x-axis always gives the number of H atoms i. The 4 different colors refer to exposure times from = 15 s (magenta), 19 s (blue), 29 s (red) to = 59 s (black).

where $Y_{\mathrm{cor}+n\mathrm{H}}$ is the integral of the peaks with $m/q \geq 300$, $Y_{\mathrm{cor}-\mathrm{C_2H}_i}$ is the integral of fragments peaks with $276 \leq m/q < 300$ and $Y_{\mathrm{fragments}}$ is the integral of all smaller fragment peaks. Y_{survival} decreases almost linearly from 1 to 0.6 when nH increases from 0 to 16. Accordingly, the fragmentation yield displayed in Fig. 7c and defined as

$$Y_{\mathrm{fragmentation}} = \frac{Y_{\mathrm{cor}-\mathrm{C_2H}_i} + Y_{\mathrm{fragments}}}{Y_{\mathrm{cor}+n\mathrm{H}} + Y_{\mathrm{cor}-\mathrm{C_2H}_i} + Y_{\mathrm{fragments}}} \quad (2)$$

exhibits an opposite trend and increases monotonically with mean hydrogenation. The relative yield of C_2H_i loss $(Y_{\mathrm{cor}-\mathrm{C_2H}_i}/(Y_{\mathrm{cor}+n\mathrm{H}} + Y_{\mathrm{cor}-\mathrm{C_2H}_i} + Y_{\mathrm{fragments}}))$ is plotted in Fig. 7d. Also here, a monotonic increase with n is evident but the yield seems to slowly saturate around $\bar{n}$ = 8. In the last panel (Fig. 7e), the ratio between C_2H_i loss and total fragmentation $(\frac{Y_{\mathrm{cor}-\mathrm{C_2H}_i}}{Y_{\mathrm{cor}-\mathrm{C_2H}_i} + Y_{\mathrm{fragments}}})$ is displayed. Here, the decrease at very low $\bar{n}$ is not reliable as it reflects a ratio between two very small numbers. The ratio is then increasing up to nH = 8 where is saturates at about 0.25.

3 Theoretical calculations

3.1 Methods

All simulations have been performed within the Born Oppenheimer approximation with on the fly computation of the potential energy. The level of theory should allow for description of chemical reactivity while conserving a reasonable computational cost to provide statistically relevant results. In this context, Density Functional based Tight Binding (DFTB),[24,25] an approximated DFT scheme whose efficiency relies on the use of parameterized integrals, is particularly well suited. We have used the Self Consistent Charge formulation[26] of DFTB as implemented in the deMonNano[27] code with the mio set of parameters.[26] DFTB has been shown to provide a reasonable description of PAH systems even when they undergo major internal rearrangement[28] or dissociation.[29]

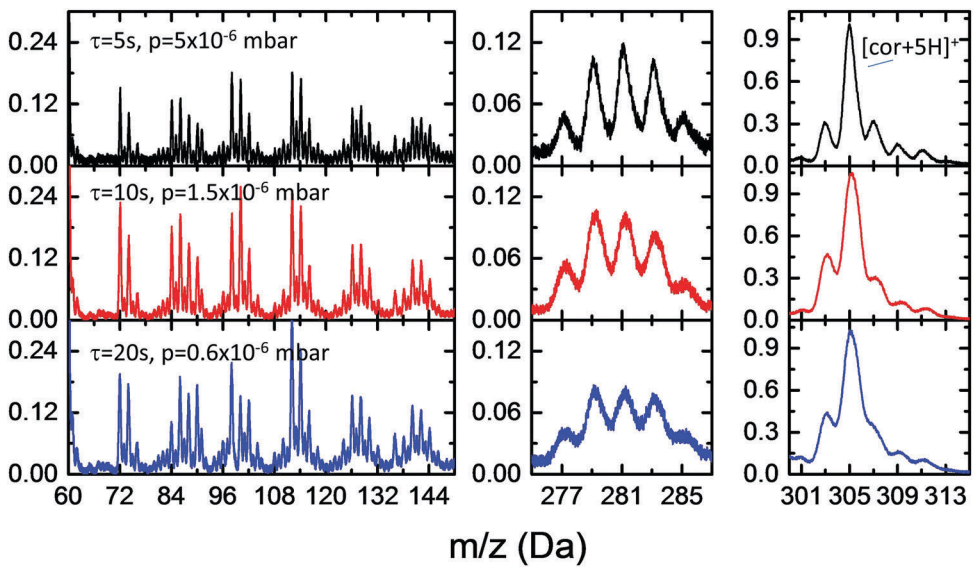

Fig. 6 Hydrogenation (right panel), C_2H_2 loss (middle panel) and multifragmentation (left panel) for τ_{exp} = 5 s/p = 5 × 10^{-6} mbar (top) τ_{exp} = 10 s/p = 1.5 × 10^{-6} mbar (middle) and τ_{exp} = 20 s/p = 0.7 × 10^{-6} mbar (bottom). All spectra are normalized to the $[C_{24}H_{12} + 5H]^+$ peak.

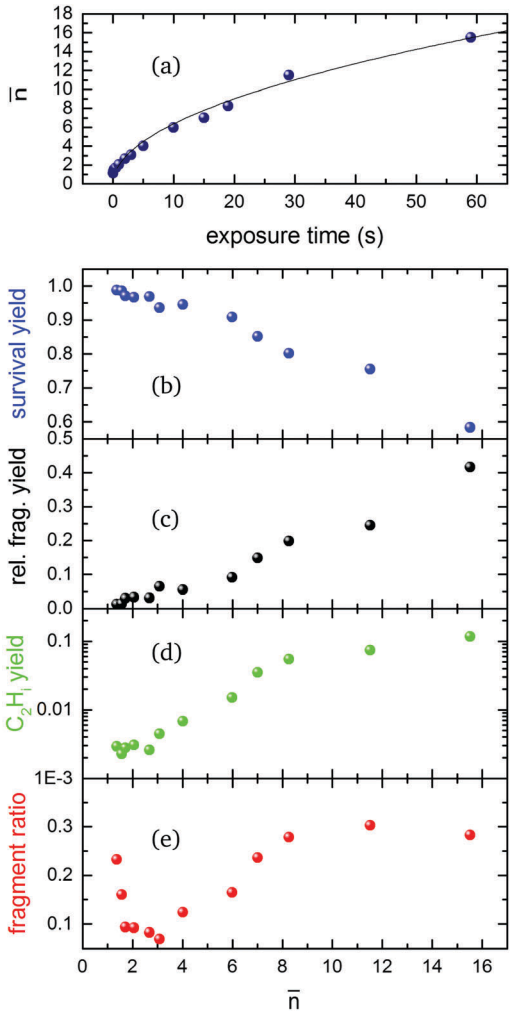

Fig. 7 (a) Mean hydrogenation $\bar{n}$ as a function of exposure time. (b–d) Display the molecular survival yield, relative fragmentation yield and C_2H_i-loss yield as a function of $\bar{n}$, respectively. (e) Ratio between fragmentation and C_2H_i loss.

Modeling the complete duration of the experiment (up to one minute) is obviously out of reach with MD/DFTB simulations. Besides, modeling the collision of a H atom with a PAH^+ ion is a challenge due to the difficulty to obtain an accurate potential energy surface for the H atom approaching PAH^+. As an alternative, the following strategy has been used to mimic the experimental results. MD simulations were initiated for coronene in various hydrogenation degrees $[C_{24}H_{12} + nH]^+$ with $n = 0$–24. For any given nH, we calculated 200 MD trajectories in the microcanonical ensemble starting from an initial geometry as obtained from previous DFT calculations[11] and reoptimized at the DFTB level. The initial vibrational excitation energy was randomly chosen within a given energy distribution discussed in the following and distributed randomly over all degrees of freedom. The time-step of the simulation was 0.5 fs and the MDs were followed for 100 ps. The total simulation time was divided into 400 segments of 250 fs duration. Upon completion of every segment, the geometry of the system was analyzed to detect possible fragmentation. In case of fragmentation, the single positive charge was arbitrarily assigned to the largest fragment. We note that Simon *et al.*[29] showed that constraining the charge to be localized on the heaviest fragment produces similar results as simulations without any constraint for dissociation PAH cations. Only this fragment was considered in the subsequent segments, as only charged fragments are detected experimentally. Overall, for a given hydrogenation state n with its well defined initial vibrational energy distribution, the masses of the final cationic fragments were retrieved for the 200 computed trajectories, resulting in a histogram-type mass spectrum.

The optimum choice of the initial energy distribution is not obvious as the competition between the increase of the internal energy due to hydrogen adsorption (between 1.9 and 3.6 eV[11]) and the different cooling processes is not known. We decided to investigate several model scenarios. (i) The incremental energy case: cooling processes are neglected and the internal energy of $[C_{24}H_{12} + nH]^+$ is taken as the sum of the binding energies corresponding to the n successive attachments of atomic hydrogen on to coronene. The resulting initial vibrational excitation energies are very high, in particular for large n. Fig. 8 gives these energies for $n = 0$ (black), $n = 12$ (red) and $n = 24$ (blue) as vertical bars. The non-zero energy at $n = 0$ reflects the thermal excitation energy at $T = 300$ K. (ii) The Boltzmann scenario: we assume thermal equilibrium in the experiment. Initial vibrational energies are taken from a Boltzmann distribution at an arbitrary temperature $T = 3500$ K. The choice of such high temperature was driven to include high energy dissociation as existing in the first scenario for highly hydrogenated coronene. The distributions for $n = 0$ (black) $n = 12$ (red) and $n = 24$ (blue) are shown for $T = 3500$ K in Fig. 8 as thick lines. For comparative reasons, we also performed simulations with a

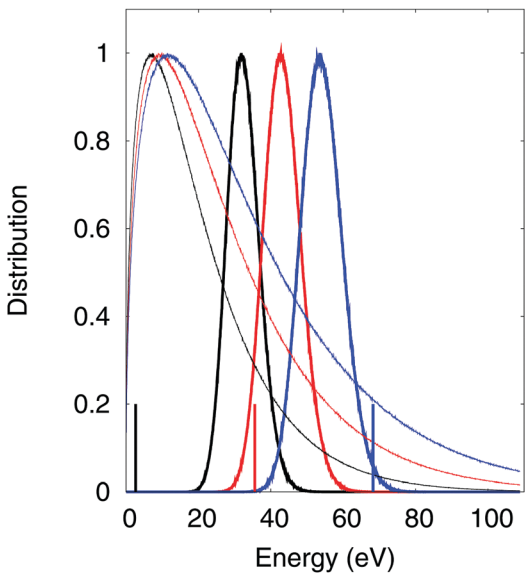

Fig. 8 Initial energy distribution in $C_{24}H_{12}$ (black), $C_{24}H_{12+12}$ (red) and $C_{24}H_{12+24}$ (blue) for the different investigated cases: Boltzmann scenario at 3500 K (thick line), broad scenario (thin line) and increment scenario (vertical bars).

Boltzmann distribution at a lower temperature T = 3000 K. (iii) The broad energy scenario which was designed such that its maximum is located at low energies while its tail covers a wide energy range. The expression of this distribution is given in Appendix A.1. This distribution is derived empirically to mimic a competition between heating and cooling processes which may result in a broadening of the energy distribution with respect to a Boltzmann distribution. Fig. 8 shows this distribution for n = 0 (black) n = 12 (red) and n = 24 (blue) as solid lines. (iv) In the last scenario, we have assumed that the energy distribution gradually changes from a combination of broad scenario (ii) at T = 3000 K and increment (i) scenario at low n to a purely broad (iii) distribution for high n. To do so, we defined a function to weight the contribution of the three scenarios as a function of n. This is detailed in Appendix A.2.

In the following the four initial energy distributions (i–iv) will be referred to as "Inc." (incremental energy case, i), "Boltz." (Boltzmann distribution centered at 3500 K and 3000 K, ii), "Broad" (broad energy distribution, iii) and "Comb." (Combination case, iv). Independent simulations have been performed for the energy distribution scenarios, except for the Comb. case which has been reconstructed from the mass spectra obtained from the other simulations.

3.2 Simulation results *vs.* experimental data

In Fig. 9, we show the full mass spectra for the different initial energy distributions, assuming an equal initial population of all superhydrogenation stages n = 0–24. Considering the Inc. distribution (Fig. 9 top panel), the mass spectrum shows that superhydrogenation is possible up to 10 extra H atoms. The fragmentation processes result in a distribution of masses over the entire range (from 0 to 300 Da). In particular, many fragments in the lower masses range (below 100 Da) are produced. For the Boltz. distributions (Fig. 9 second and third panels), superhydrogenation is very weakly seen in the mass spectrum. The masses of the different fragments are distributed quite similarly over the whole mass domain, from 30 to 300 Da. When a Broad or Combined distribution is considered (Fig. 9 two bottom panels), superhydrogenated coronene cations are observed while at the same time mainly low mass fragments are produced (less than 100 Da). The bimodal pattern, also observed experimentally, obtained from the Broad and Combined simulations is due to (i) low initial energies for

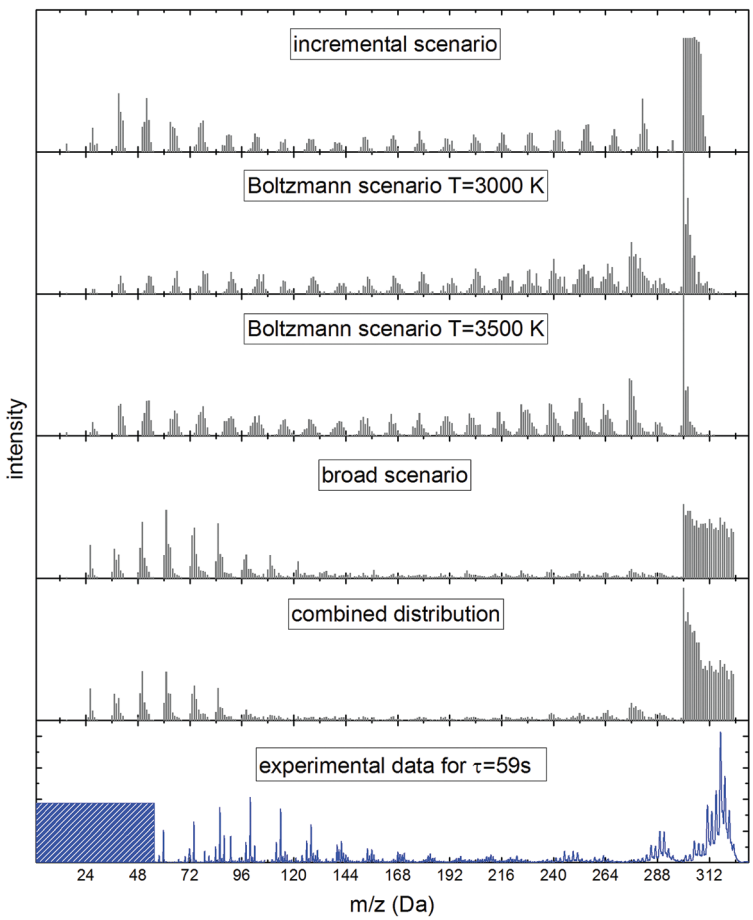

Fig. 9 Mass spectra obtained by summing the simulation results starting from $C_{24}H_{12+n}$ with n ranging from 1 to 24, with initial energy distribution corresponding to the energy increment, Boltzmann, broad and combination scenarios. Experimental data for τ = 59 s is shown for comparison (from Fig. 2). The shaded blue region is experimentally inaccessible.

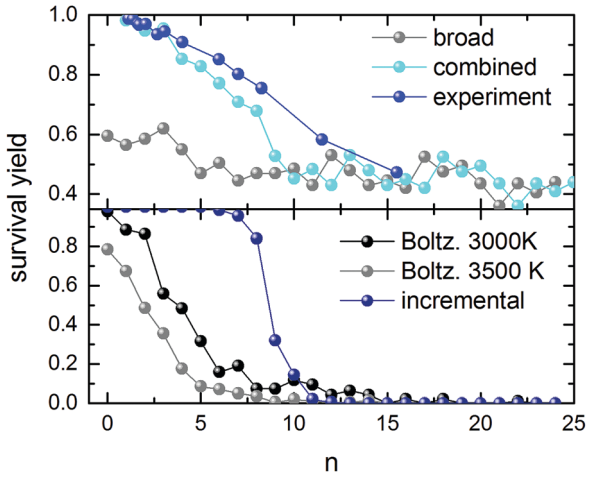

Fig. 10 Molecular survival yield as a function of the initial superhydrogenation degree n. Top: Simulation results for the broad and the combined scenarios in comparison to the experimental data from Fig. 7. Bottom: Results for the Boltzmann and the incremental energy distributions.

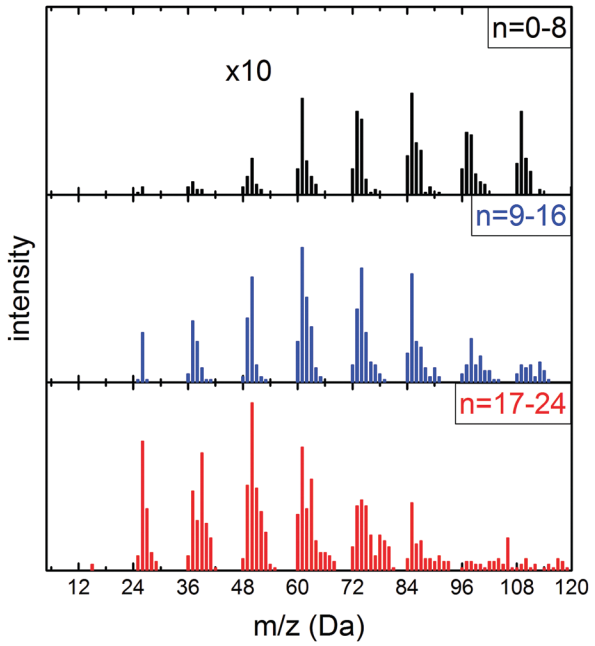

Fig. 11 Mass spectra obtained by summing the simulation results starting from $C_{24}H_{12+n}$ with n = 0–8 (top), n = 9–16 (middle) and n = 17–24 (bottom) with initial energy distribution corresponding to the broad scenario. The thin lines with an offset represent the experimental spectra for τ = 10, 29 and 59 s from Fig. 2.

which no destruction is observed (initial superhydrogenated PAHs survive) and (ii) high initial energy leading to small fragments.

We discuss now in more detail the fraction of surviving molecules. Fig. 10 reports the percentage of "surviving" molecular ions (see eqn (1)) as a function of initial n. It appears that the surviving probability decreases when the initial superhydrogenation degree increases. In the Inc. and Boltz. cases, almost all coronene ions with an initial $n > 10$ do fragment. The transition from survival to fragmentation is very sharp in the Inc. case and less in the Boltz. cases (0–10), which is not what is seen experimentally. For the Broad energy distribution the survival percentage changes gradually from about 60% to 40% when n increases from 0 to 16. As expected, the combination scenario resembles the Inc./Boltz results for low n, while for high n, it becomes similar to the Broad case. This scenario provides survival yields close to the ones derived in the experiments.

One should note at this point that structural weakening of highly hydrogenated coronene is expected as each additional H atom reduces the delocalized π system (especially when bonding with a non-peripheral carbon atom). This results in deformation of the plane and a weakening of C–C bond energies. On top of this, the initial energy distribution is shifted to higher energies. This is particularly true in the Inc. scenario for which the fully hydrogenated coronene contains initially ~70 eV. In the Boltz. simulation, the mean energy per mode is the same for all hydrogenation degrees, but the total available energy increases with the system's size. From this result, we may infer the general trend that, for the coronene cation, a larger hydrogenation degree leads to a decrease in stability with respect to thermal dissociation. Although strictly speaking, this conclusion is only confirmed for the initial energy distributions under study here, most likely this finding is generally valid, as it is consistent with previous experiments and calculations by Wolf *et al.*[13] and Gatchell *et al.*[14] who observed that superhydrogenation decreases pyrene stability with respect to collision induced dissociation (experiment) and thermal dissociation (theory).

Let us mention at this point that, considering that the experimental spectra exhibit a bimodal distribution (superhydrogenation and fragments with small masses, Fig. 9 bottom), two features only present in the broad and combined scenario, these two scenarios are considered the most promising and will be the only ones further discussed.

We now investigate how the initial hydrogenation influences the details of the fragmentation process, and in particular, the sizes of the fragments in specific regions of the mass spectra. Fig. 11 (broad distribution) and 12 (combined distribution) highlight the small fragments region (up to 120 Da) separating the fragments produced by coronene with a low (0–8), intermediate (9–16) and high (17–24) initial superhydrogenation degree. It appears that highly hydrogenated coronene produce smaller fragments, as observed experimentally (Fig. 4), which is in agreement with their lower stability. The opposite trend is observed in the regions corresponding to C_2H_i-loss (270–295 Da, *cf.* Fig. 13 and 14), the more hydrogenated species producing the larger fragments, in agreement with experimental results (Fig. 3). This is related to the fact that superhydrogenated coronene produces superhydrogenated C_2H_i-loss fragments.

The evolution of the C_2H_i-loss intensity is represented in Fig. 15. Note that the n on the x-axis represents the simulation results for an interval of superhydrogenation degrees n ([n − 2:n + 2]). This presentation aims at mimicking the experimental distribution,

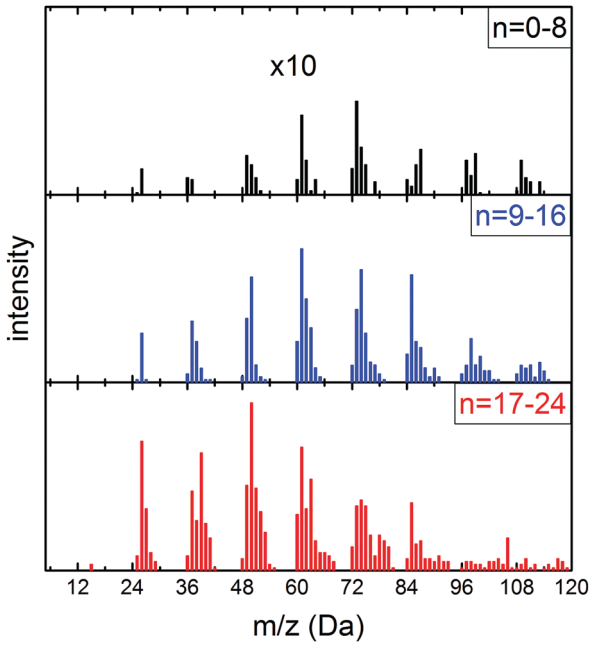

Fig. 12 Mass spectra obtained by summing the simulation results starting from $C_{24}H_{12+n}$ with n = 0–8 (top), n = 9–16 (middle) and n = 17–24 (bottom) with initial energy distribution corresponding to the combination scenario.

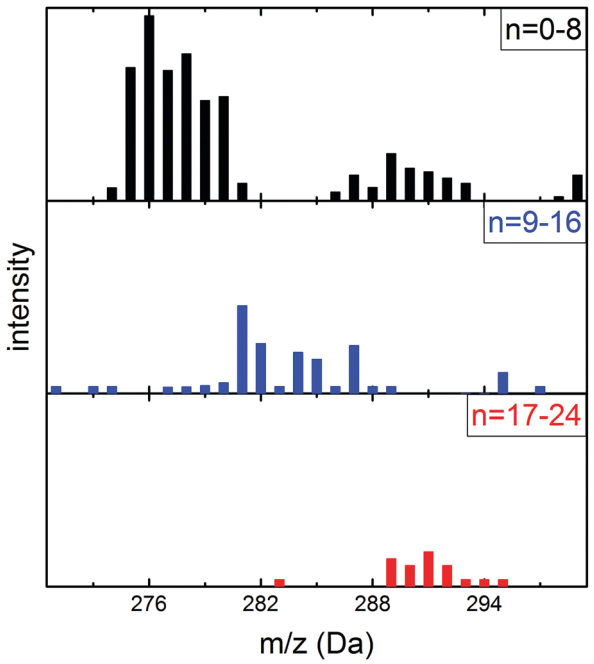

Fig. 13 Mass spectra obtained by summing the simulation results starting from $C_{24}H_{12+n}$ with n = 0–8 (top), n = 9–16 (middle) and n = 17–14 (bottom) with initial energy distribution corresponding to the broad scenario.

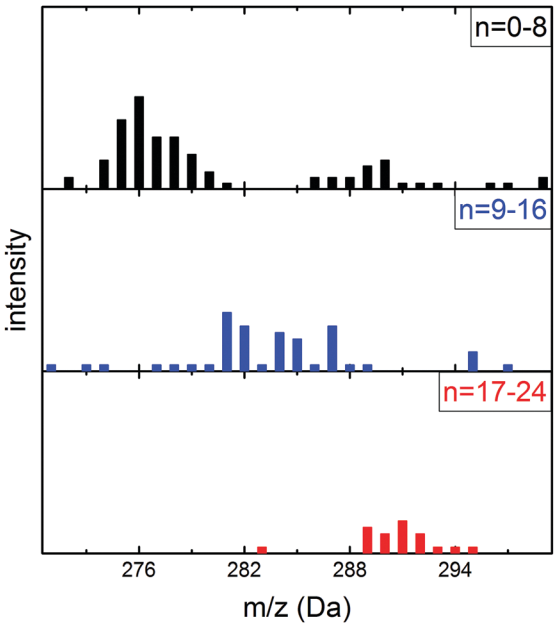

Fig. 14 Mass spectra obtained by summing the simulation results starting from $C_{24}H_{12+n}$ with n = 0–8 (top), n = 9–16 (middle) and n = 17–14 (bottom) with initial energy distribution corresponding to the combination scenario.

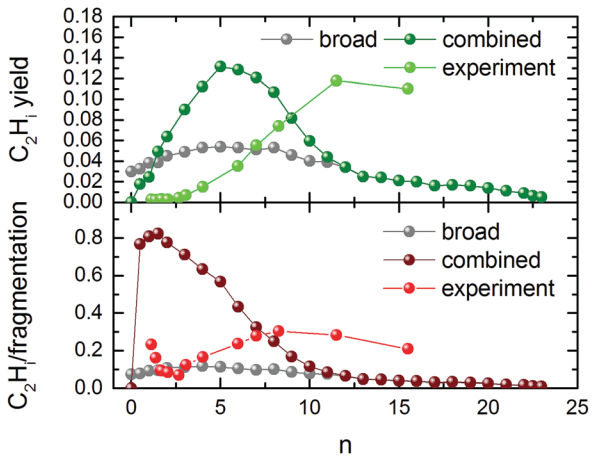

Fig. 15 The yields of $C_{24-2}H_j$ molecules (*i.e.* C_2H_i-loss), relative to the total number of molecules (top) or to the total number of fragments that lost at least one C atom (bottom), both for the broad scenario and for the combined distribution. For each initial superhydrogenation value n, an interval of superhydrogenations is considered to resemble the mean hydrogenation $\bar{n}$ used in the experimental section and in particular Fig. 7.

which at a given time does not present a unique hydrogenation degree for the parents. In the two scenarios presented, the loss of C_2H_i increases with the coronene hydrogenation degree, reaches a maximum at around 5 and then decreases. However, the experimental data show that the C_2H_i loss increases until a hydrogenation degree of 11 is reached. Coronene cations with few extra H atoms have more chance to fragment by losing a C_2H_i fragment than highly hydrogenated ones that disintegrate into small fragments. This accounts for the evolution of the C_2H_i loss channel with respect to other fragmentation processes (Fig. 15 bottom). We note that the C_2H_i loss channel is much favored in the combination scenario with respect to the broad scenario, reaching more than 75% of fragments for low hydrogenation degrees. The C_2H_i loss channel compared to

other fragmentation channels is quantitatively not well described by our simulations.

Finally, one should also mention that the simulations were not able at reproducing the odd–even patterns observed experimentally. Two fundamental issues could be the reason for the above mentioned discrepancies. First of all, the simulation does not take into account the hydrogenation process itself. Mass spectral features that reflect the hydrogenation process, such as the odd–even oscillations in $[C_{24}H_{12} + nH]^+$ yields which are due to oscillations in reaction barrier heights, thus cannot be reproduced. This also holds for hydrogenation of fragmentation products, *e.g.* those formed by C_2H_i-loss. Here, fragment hydrogenation could lead to stabilization of fragments, preventing further fragmentation. Secondly, the simulations only follow the dynamics of the system for the first 100 ps, *i.e.* all fragmentation processes that occur on longer timescales are neglected. In principle, the use of statistical approaches (RRKM, statistical collision theory) could be a way to access these long term evolutions. Unfortunately, they are hardly applicable here due to the large number of possible isomerisation/dissociation channels to investigate.

4 Radiative cooling

A key quantity for the simulation is the amount of excitation energy that is lost between subsequent collisions with H atoms. In an RF ion trap, intact molecular ions can be cooled (i) collisionally and (ii) radiatively. Collisional cooling is a key process in ion trap mass spectrometry, where bath gas (usually He at about 10^{-3} mbar) collisions are employed to reduce trapped ion kinetic energies. The reduction in kinetic energy is accompanied by internal cooling. Glish and coworkers[30] have shown that the effect of collisional cooling on trapped ion internal energies vanishes in the low 10^{-4} mbar pressure range. In our experiments, H_2 and H from the atomic H source increase the pressure in the ion trap only up to the range of 5×10^{-6} mbar, *i.e.* collisional cooling is considered negligible. As in most astrophysically relevant environments, molecular ions can only exchange energy with their environment through radiative processes. It has long been assumed that vibrationally hot molecular ions radiatively cool by means of photon emission from infrared active vibrational modes, with radiative lifetimes τ_{rad} in the range of several seconds for PAH cations.[31] In this framework, a primary electronic excitation – for instance by UV or visible photoabsorption – is first transformed into vibrational excitation by means of internal conversion (IC), before IR cooling sets in. Already in 1988, Léger *et al.*[32] have proposed a second and much faster radiative cooling mechanism, active for particularly high internal excitation: the so-called Poincaré fluorescence occurs after inverse internal conversion, where an electronically excited state is populated thermally. For anthracene cations, Poincaré fluorescence was first observed in a multiphoton dissociation experiment by Boissel *et al.*[33] who observed ''conventional'' IR cooling with a rate of $k_{ir} = 2\ s^{-1}$ up to internal energies of 4 eV and an exponential increase of the rate with internal energy above. Using an electrostatic storage ring, Martin *et al.*[34,35] have directly determined the Poincaré fluorescence rate $k_{fluoresc} \approx 250\ s^{-1}$ for anthracene cations at internal energies of 6.8 eV.

In our work, experiment and simulation focus on the competition between cooling and fragmentation of coronene cations which have been heated by successive collisions with H atoms. As fragmentation requires very high internal energies cooling should be dominated by Poincaré fluorescence. The emission rate of the fluorescence photons then simply is the product of the Einstein coefficient for the transition and the population of the respective excited state. Cooling by Poincaré fluorescence is thus closely linked to molecular electronic structure, not only *via* the Einstein coefficient of the respective transition, but also *via* the excitation energy, as this energy has to be populated thermally. This has profound implications for Poincaré cooling of $[C_{24}H_{12} + nH]^+$, as TD-DFT calculations have shown that the HOMO–LUMO gap of PAH cations generally decreases sharply upon hydrogenation and electronic emission spectra strongly shift to longer wavelengths.[36] Coronene$^+$ is thus expected to cool much slower as compared to $[C_{24}H_{12} + nH]^+$ ($nH > 0$). It is very likely that this effect stabilizes the hydrogenated systems against fragmentation. For fragment cations, on the other hand, the situation is much more complex. Many studies have already shown that PAH fragmentation after energetic interactions[21,37] can lead to hydrocarbon chains, ring and clusters that vary strongly in size as well as geometric and electronic structure. Very recently, this has been illustrated by Hansen and co-workers[38] who experimentally investigated cooling of C_6^- and C_6H^-. With its open shell structure, C_6^- cools predominantly by extremely fast de-excitation from thermally populated low lying electronically excited states. For closed shell C_6H^-, the much larger HOMO–LUMO gap prevents thermal population of electronically excited states and the fast cooling channel is accordingly closed.

5 Conclusions

We have studied experimentally the hydrogenation of coronene cations in a radiofrequency ion trap using tandem mass spectrometry. The mass spectra at high masses (from 300 until 324 Da) reveal that the hydrogenation degree of coronene cations increases with increasing H-exposure time, until full coverage is obtained. Also, it shows that odd m/z (close shell systems) are dominating the mass spectra, highlighting the alternance between radical and close shell systems. At low masses, on the other hand, different fragments from coronene cations can be observed highlighting that the energy deposited by H-addition results in different loss channels. Masses between 274 $(C_{24}H_{12}–C_2H_2)^+$ and 298 $(C_{24}H_{12} + 24H–C_2H_2)^+$ are due to the C_2H_2-loss channel, while lower masses (between 60 and 180 Da) are associated to smaller fragments such as $C_6H_2^+$, $C_7H_2^+$, $C_8H_4^+$, $C_9H_6^+$, $C_{10}H_4^+$ and $C_{11}H_9^+$. With increasing H-exposure time, the fragment masses shift from higher masses to lower masses. Molecular dynamics calculations have been

performed to study the fragmentation patterns seen experimentally. These simulations were initiated with various hydrogenation states for the coronene cations. The results show the different fragments from the coronene cations with various numbers of extra H atoms. The fact that coronene cations can be fully hydrogenated but at the same time fragments contain precious information on how the energy deposited is dissipated. If all cooling processes are neglected, the coronene cations will completely fragment after the addition of a maximum of 10 H atoms. Higher hydrogenated states should therefore not be observed in the simulations. Assuming that the energy increased due to H-addition follows a broad distribution centered at reduced energies (to simulate that the system is allowed to cool in between the addition of hydrogens), the coronene cations can be fully hydrogenated and fragmentations is also reproduced. However, to reproduce the fact that the survival of coronene cations decreases slowly with the number of attached H atoms, the increase of energy with H addition should be large for low hydrogenation degree (no cooling is considered) while the increase of energy should be much less for high hydrogenation degree. This combined scenario reproduces the main experimental results: (i) superhydrogenated coronene cations survive (until full coverage) (ii) fragmentation into small mass fragments is observed (iii) the survival of coronene cations decreases slowly with hydrogenation. On a minor note, some trends seen in the experiments are still not fully grasped by the calculations as the different fragmentation channels are not well reproduced in the theoretical spectra, which may suffer from the lack of long term dissociation events.

Conflicts of interest

There are no conflicts to declare.

Appendix A

A.1 Broad energy distribution

The broad energy has been defined to reproduce at a given temperature a distribution of the total energy over a larger ranges than it would be in the case of a Boltzman distribution. The energy distribution for a system with p degrees of freedom is given by $P(E) = P(t = 2E/p)$ where the distribution probability of t is given by a gamma distribution of scale kT with $T = 3000$ K and a scale of 1.5. Note that this expression is empirical, only derived to present a large energy distribution and, of course, should never be identified to that of a Boltzman distribution of p atoms at $T = 3000$ K.

A.2 The combination scenario

As explained in the main text, the combination distribution is defined to mimic an evolution of the initial energy distribution for the MD simulation that is close to the Inc. and Boltz ($T = 3000$ K) scenarios for low hydrogenation degrees and close to the Broad scenario case for large hydrogenation degrees. We have derived the following empirical formulas for the weighting of the three contributions to the Comb. case as a function of the superhydrogenation degree nH.

$$w_{\mathrm{B3000K}}(n) = \frac{1}{6}(1 - \mathrm{erf}(n - 9))$$

$$w_{\mathrm{Inc.}}(n) = 2 \times w_{\mathrm{B3000K}}(n)$$

$$w_{\mathrm{Broad}}(n) = 1 - w_{\mathrm{Inc.}}(n) - w_{\mathrm{B3000K}}(n)$$

The mass spectrum of the combination ($\mathrm{Ms_{Comb.}}$) scenario is built from the mass spectra of the three involved distributions:

$$\mathrm{Ms_{Comb.}} = w_{\mathrm{B3000K}}(n)\mathrm{Ms_{B3000K}}(n) + w_{\mathrm{Inc.}}(n)\mathrm{Ms_{Inc.}}(n) + w_{\mathrm{Broad}}(n)\mathrm{Ms_{Broad}}(n)$$

Acknowledgements

The authors would like to thank Fernand Spiegelman for fruitful discussions. The authors acknowledge the computing facility CALMIP for allocation of computer resources.

References

1 D. C. Elias, R. R. Nair, T. M. G. Mohiuddin, P. B. S. V. Morozov, M. P. Halsall, A. C. Ferrari, D. W. Boukhvalov, M. I. Katsnelson, A. K. Geim and K. S. Novoselov, *Science*, 2009, **323**, 610.
2 L. J. Allamandola, A. G. G. M. Tielens and J. Barker, *Astrophys. J.*, 1985, **290**, L25–L28.
3 A. Léger and J. L. Puget, *Astron. Astrophys.*, 1984, **137**, L5–L8.
4 C. Boersma, J. Bregman and L. J. Allamandola, *Astrophys. J.*, 2015, **806**, 121.
5 M. J. F. Rosenberg, O. Berne and C. Boersma, *Astron. Astrophys.*, 2014, **566**, L4.
6 E. Habart, F. Boulanger, L. Verstraete, C. M. Walmsley and G. P. des Forets, *Astron. Astrophys.*, 2004, **414**, 531–544.
7 S. Cazaux and M. Spaans, *Astron. Astrophys.*, 2009, **496**, 365–374.
8 C. W. Bauschlicher, *Astrophys. J.*, 1998, **509**, L125–L127.
9 J. D. Thrower, B. Jorgensen, E. E. Friis, S. Baouche, V. Mennella, A. C. Luntz, M. Andersen, B. Hammer and L. Hornekaer, *Astrophys. J.*, 2012, **752**, 3.
10 L. Boschman, G. Reitsma, S. Cazaux, T. Schlathölter, R. Hoekstra, M. Spaans and O. Gonzalez-Magaña, *Astrophys. J., Lett.*, 2012, **761**, L33.
11 S. Cazaux, L. Boschman, N. Rougeau, G. Reitsma, R. Hoekstra, D. Teillet-Billy, S. Morisset, M. Spaans and T. Schlathölter, *Sci. Rep.*, 2016, **6**, 19835.
12 G. Reitsma, L. Boschman, M. J. Deuzeman, O. Gonzalez-Magaña, S. Hoekstra, S. Cazaux, R. Hoekstra and T. Schlathölter, *Phys. Rev. Lett.*, 2014, **113**, 053002.
13 M. Wolf, L. Giacomozzi, M. Gatchell, N. de Ruette, M. H. Stockett, H. T. Schmidt, H. Cederquist and H. Zettergren, *Eur. Phys. J. D*, 2016, **70**, 85.
14 M. Gatchell, M. H. Stockett, N. de Ruette, T. Chen, L. Giacomozzi, R. F. Nascimento, M. Wolf, E. K. Anderson,

R. Delaunay, V. Vizcaino, P. Rousseau, L. Adoui, B. A. Huber, H. T. Schmidt, H. Zettergren and H. Cederquist, *Phys. Rev. A: At., Mol., Opt. Phys.*, 2015, **92**, 050702.

15 S. Bari, O. Gonzalez-Magaña, G. Reitsma, R. Hoekstra, J. Werner, S. Schippers and T. Schlathölter, *J. Chem. Phys.*, 2011, **134**, 024314.

16 E. P. Maziarz, G. A. Baker and T. D. Wood, *Can. J. Chem.*, 2005, **83**, 1871–1877.

17 J. Slevin and W. Stirling, *Rev. Sci. Instrum.*, 1981, **52**, 1780–1782.

18 R. Hoekstra, F. J. de Heer and R. Morgenstern, *J. Phys. B: At., Mol. Opt. Phys.*, 1991, **24**, 4025–4048.

19 F. W. Bliek, G. R. Woestenenk, R. Hoekstra and R. Morgenstern, *Phys. Rev. A: At., Mol., Opt. Phys.*, 1998, **57**, 221–226.

20 H. H. Jochims, E. Rühl, H. Baumgärtel, S. Tobita and S. Leach, *Astrophys. J.*, 1994, **420**, 307.

21 J. J. U. Postma, S. Bari, R. Hoekstra, A. G. G. M. Tielens and T. Schlathölter, *Astrophys. J.*, 2010, **708**, 435.

22 T. Chen, M. Gatchell, M. H. Stockett, R. Delaunay, A. Domaracka, E. R. Micelotta, A. G. G. M. Tielens, P. Rousseau, L. Adoui, B. A. Huber, H. T. Schmidt, H. Cederquist and H. Zettergren, *J. Chem. Phys.*, 2015, **142**, 144305.

23 M. H. Stockett, M. Gatchell, T. Chen, N. de Ruette, L. Giacomozzi, M. Wolf, H. T. Schmidt, H. Zettergren and H. Cederquist, *J. Phys. Chem. Lett.*, 2015, **6**, 4504–4509.

24 D. Porezag, T. Frauenheim, T. Kohler, G. Seifert and R. Kaschner, *Phys. Rev. B: Condens. Matter Mater. Phys.*, 1995, **51**, 12947–12957.

25 G. Seifert, D. Porezag and T. Frauenheim, *Int. J. Quantum Chem.*, 1996, **58**, 185–192.

26 M. Elstner, D. Porezag, G. Jungnickel, J. Elsner, M. Haugk, T. Frauenheim, S. Suhai and G. Seifert, *Phys. Rev. B: Condens. Matter Mater. Phys.*, 1998, **58**, 7260–7268.

27 T. Heine, M. Rapacioli, S. Patchkovskii, J. Frenzel, A. M. Köster, P. Calaminici, H. A. Duarte, S. Escalante, R. Flores-Moreno, A. Goursot, J. U. Reveles, D. R. Salahub and A. Vela, *deMon-Nano*, 2016.

28 M. Rapacioli, A. Simon, C. C. M. Marshall, J. Cuny, D. Kokkin, F. Spiegelman and C. Jobin, *J. Phys. Chem. A*, 2015, **119**, 12845–12854.

29 A. Simon, M. Rapacioli, G. Rouaut, G. Trinquier and F. X. Gadea, *Philos. Trans. R. Soc., A*, 2017, **375**, 20160195.

30 D. M. Black, A. H. Payne and G. L. Glish, *J. Am. Soc. Mass Spectrom*, 2006, **17**, 932–938.

31 R. C. Dunbar, *Mass Spectrom. Rev.*, 1992, **11**, 309–339.

32 A. Léger, P. Boissel and L. d'Hendecourt, *Phys. Rev. Lett.*, 1988, **60**, 921–924.

33 P. Boissel, P. de Parseval, P. Marty and G. Lefevre, *J. Chem. Phys.*, 1997, **106**, 4973–4984.

34 S. Martin, J. Bernard, R. Bredy, B. Concina, C. Joblin, M. Ji, C. Ortega and L. Chen, *Phys. Rev. Lett.*, 2013, **110**, 063003.

35 S. Martin, M. Ji, J. Bernard, R. Bredy, B. Concina, A. R. Allouche, C. Joblin, C. Ortega, G. Montagne, A. Cassimi, Y. Ngono-Ravache and L. Chen, *Phys. Rev. A: At., Mol., Opt. Phys.*, 2015, **92**, 053425.

36 M. Hammonds, A. Pathak and P. J. Sarre, *Phys. Chem. Chem. Phys.*, 2009, **11**, 4458–4464.

37 A. Lawicki, A. I. S. Holm, P. Rousseau, M. Capron, R. Maisonny, S. Maclot, F. Seitz, H. A. B. Johansson, S. Rosen, H. T. Schmidt, H. Zettergren, B. Manil, H. Cederquist, L. Adoui and B. A. Huber, *Phys. Rev. A: At., Mol., Opt. Phys.*, 2011, **83**, 022704.

38 G. Ito, T. Furukawa, H. Tanuma, J. Matsumoto, H. Shiromaru, T. Majima, M. Goto, T. Azuma and K. Hansen, *Phys. Rev. Lett.*, 2014, **112**, 183001.

